

Strongly-Mismatched Regime of Self-guided Laser-driven Nonlinear Plasma-Wave based Electron Acceleration

Aakash A. Sahai¹

¹*Department of Physics and John Adams Institute for Accelerator Science, Blackett Laboratory, Imperial College London, SW7 2AZ, United Kingdom**

A strongly mismatched regime of laser-plasma acceleration using a self-guided laser-driven bubble-shaped nonlinear plasma electron wave is introduced and modeled. In this regime the radial envelope of a laser-pulse incident at the plasma entrance is mismatched to the nonlinear electron response excited by it, in contrast to the established understanding. A nonlinear laser envelope equation is derived to show that as the strength of the mismatch is increased, the envelope oscillations steepen and become increasingly asymmetric, exhibiting shorter and tighter radial squeeze phases. The sharply increasing intensity in a shortened squeeze phase results in the slicing of the longitudinal laser envelope, driving a strong optical-shock. The optical shock results in an elongating bubble shape with significantly higher peak plasma fields and a novel self-injection mechanism which produces beams of high transverse qualities. The behavior of peak beam energies from Particle-In-Cell simulations and self-guided multi-GeV experimental data are in good agreement with the predictions of an adjusted- a_0 model and significantly exceed the matched regime predictions.

I. INTRODUCTION

Plasma-based acceleration structures [1] using self-guided laser-driven non-linear plasma electron density waves with a “bubble”-like shape [2–5] have been extensively modeled in a “matched” regime. Maximum gain in energy is shown to be possible only if the incident spot-size of the laser is equal to the characteristic size of the non-linear electron response excited by it in the plasma. The laser satisfies temporal matching with its pulse length being around a bubble radius. This initial condition minimizes the radial envelope oscillations and has been argued to be indispensable for maintaining the stability of the dimensions of the bubble over the acceleration length. It is further argued that it is the stability of the acceleration structure that makes nearly a bubble radius available for energy gain of the beam while preserving the transverse phase-space. Thus spot-size matching is considered critical for optimizing both the beam energy gain and the phase-space properties.

In this work, contrary to the established understanding that highest beam energies are attainable only in a matched regime, a novel mis-matched regime of self-guided laser-plasma accelerator is introduced for the first time and shown to be more effective than the matched regime. The laser focal spot-size in this regime is much larger than dictated by the matched condition. We also show that in this regime, a high charge self-injected beam of high transverse quality is accelerated due to a novel injection mechanism.

Although many groundbreaking experimental data have an underlying signature of the effectiveness of the mismatched regime developed here, no earlier work has investigated the details of the physical mechanisms underlying the acceleration process.

There are two primary motivations for studying the mis-matched regime. Firstly, a larger vacuum focal spot-size at a given laser power is known to produce higher “mode-quality” far-field laser focal-spots (low beam propagation factor or \mathcal{M}^2 -number or TEM_{00} -times diffraction-limited number [6]). This is because a larger vacuum focal spot-size is less affected by various aberrations [6]. High mode-quality is not equivalent to maximizing the intensity percentage within the focal-spot, as characterized by the Strehl ratio [7]. This is because of the well-defined “no- TEM_{00} gaussian” problem [6]. Secondly, the plasma electrons trajectories that violate the orderly oscillations supporting the wave get trapped and accelerated by the wave. In the mismatched regime, large-scale driver envelope modulations [8–12] produce a higher degree of violations, this results in a higher “self-injected” charge.

The laser-plasma interaction effects investigated here are in the self-guided bubble regime of plasma wave [2–5]. In a plasma with a homogeneous electron density, n_0 , self-guiding of a laser with predominantly TEM_{00} -mode over multiple Rayleigh lengths, $Z_R \equiv \pi w_0^2/\lambda_0 = \pi W_0^2/(\mathcal{M}^2 \lambda_0)$ (λ_0 is the central wavelength of the laser and w_0 is the spot-size of TEM_{00} mode and W_0 is the measured spot-size) requires the evacuation of electrons, referred to as cavitation [9, 10]. This happens when the laser power, P exceeds a critical power, $P_c = 17.4 \times 10^9 (\omega_0/\omega_{pe})^2$ (ω_0 is laser angular frequency and $\omega_{pe} = \sqrt{4\pi n_0 e^2/m_e}$ is the plasma angular frequency). For $P \geq P_c$, refractive index shaping based upon relativistic-quiver [9, 10] and ponderomotive-channeling [11] counter the natural diffraction of a focused laser.

While cavitation occurs when $P \geq P_c$, excitation of a bubble plasma wave requires that the peak normalized laser vector potential, $a_0 \gg 1$ (where $a_0 = \max[\mathbf{eA}/m_e c^2] = 8.55 \times 10^{-10} \lambda_0 [\mu\text{m}] \sqrt{I_0 [\text{W}/\text{cm}^2]}$ the peak normalized vector potential, \mathbf{A} is the laser vector potential, I_0 is the peak intensity and λ_0 the wavelength).

* corresponding author: aakash.sahai@gmail.com

This high-intensity condition is achieved by tightly focussing a laser pulse at the plasma. In the self-guiding regime laser-driven plasma electron response maintains the laser spot-size close to the launched spot-size which when in vacuum characteristically diffracts away over Z_R .

In the bubble regime, the laser excited non-linear plasma response (electron-ion charge separation) equilibrates with the laser ponderomotive force such that the plasma-wave matched spot-size is [5][13],

$$R_{\text{bubble}} = 2\sqrt{a_0} \frac{c}{\omega_{pe}} \quad (1)$$

When a laser pulse with over-critical power is coupled into the plasma such that its waist-size $w_0 = R_{\text{bubble}}$, is related to its peak normalized vector potential a_0 by eq.1, its envelope oscillations are minimized due to the equilibrium forced by the initial conditions, this is the ‘‘matched condition’’. This matched condition on the spot-size is shown to be a critical point of bifurcation when analyzing the nonlinear envelope equation developed below. Electron energy gain in this matched regime, based upon 3D PIC simulations, scales as [13]:

$$\Delta\mathcal{E} [m_e c^2] \simeq \frac{2}{3} a_0 \left(\frac{n_c}{n_0} \right) \quad (2)$$

The laser strength parameter in eq.2, is its value in vacuum as it is launched or incident at the plasma entrance. In plasma, the value of a_0 is known to significantly vary over the acceleration length due to several non-linear laser-plasma interactions effects such as the localized variation of the wavelength profile, group velocity profile and pump depletion of the laser pulse. Thus, this equation best models a scenario where a_0 is relatively constant over the acceleration length, as is argued to be the case under a matched spot-size.

It is important to note that in the GeV-scale energy gain experiments on which our analysis is based [14, 15], mismatched regime results in the maximum gain in beam energy. In these works, during scans over density with a fixed incident laser spot-size, the beam energy gain maximizes where matched spot-size is much smaller than the incident spot-size. We show below that at higher intensities, the mismatch inflates the difference between eq.2 and the experimental data.

It is also important to note that this work directly applies to the pioneering results on self-guided laser-driven plasma-based quasi-mono-energetic electron acceleration. In [3], the incident laser intensity was $2.5 \times 10^{18} \text{Wcm}^{-2}$ ($a_0=1.1$) at $n_0 = 2 \times 10^{19} \text{cm}^{-3}$, the matched spot-size is $\simeq 3 \mu\text{m}$ whereas the launched spot-size was $\simeq 12 \mu\text{m}$ (FWHM $\simeq 20 \mu\text{m}$). The predicted energy from eq.2 is 40 MeV but experiments obtained a spectral peak at 70 MeV. Similarly in [4], the intensity was $3.2 \times 10^{18} \text{Wcm}^{-2}$ ($a_0=1.3$) at $n_0 = 6 \times 10^{18} \text{cm}^{-3}$, the matched spot-size is $\simeq 5 \mu\text{m}$ whereas the launched spot-size of $12.5 \mu\text{m}$ (FWHM $\simeq 21 \mu\text{m}$). The expected beam energy is 155 MeV but the spectral peak was at 175 MeV.

The analysis here gains additional significance due to its relevance to many other self-guiding results. Some examples are, Austin-2 GeV data [16]: $W_0 = 275 \mu\text{m}$, $a_0 = 0.6$, $n_0 = 5 \times 10^{17} \text{cm}^{-3}$ matched- $w_0 \simeq 12 \mu\text{m}$; Nebraska-0.3 GeV data [17]: $W_0 = 17 \mu\text{m}$, $a_0 = 2.2$, $n_0 = 2.5 \times 10^{18} \text{cm}^{-3}$ matched- $w_0 \simeq 10 \mu\text{m}$; Gwangju-3 GeV data [18]: $W_0 = 25.5 \mu\text{m}$, $a_0 = 5.0$, $n_0 = 5 \times 10^{17} \text{cm}^{-3}$ matched- $w_0 \simeq 20 \mu\text{m}$ and Strathclyde-125MeV data [19]: $W_0 = 20 \mu\text{m}$, $a_0 = 1.5$, $n_0 = 1 \times 10^{19} \text{cm}^{-3}$ matched- $w_0 \simeq 5 \mu\text{m}$.

A reduction in the experimental artifacts for a larger than matched-size focal spots leads to higher plasma-wave quality. Whereas a non-uniform laser focal-spot (a large \mathcal{M}^2 -number) affects the transverse characteristics of the plasma wave [20], leading to non-optimal acceleration and focusing field profiles in the plasma. This is apart from the faster laser energy loss due to the higher tendency of the higher-order modes to diffract. The quality of the plasma wave has been indirectly inferred using the laser focal profile at the plasma entrance [16] and exit [15]. The presence of multiple hot-spots in the incident focal spot may be inferred by observing the laser exit mode, as seen in Fig.3(c)-(h) in [15].

We show, using a nonlinear envelope equation of a self-guided laser driving a bubble plasma wave that the oscillations of the spot-size become increasingly asymmetric in response to an increasing degree of mismatch, with shorter (and tighter) ‘‘squeeze’’ phases and longer ‘‘relaxation’’ phases of the laser spot-size. This behavior is similar in characteristics to a ‘‘cnoidal’’ wave, whose form is given by the Jacobi elliptic function, ‘‘cn’’ [21] and is also known to be a solution of the Korteweg-de-Vries equation [22]. Such behavior is not modeled in earlier analyses of the evolution of a self-guided laser envelope [8–12]. The resulting peak intensities in the squeeze phase are much higher than that reached in the matched regime at the same intensity and the rate of change of the intensity during the shortened squeeze phase is not expected from matched regime considerations. Consequently, the laser-plasma interaction processes during the rapid spot-size squeeze events dictate the physical mechanisms underlying the acceleration process.

Using Particle-In-Cell (PIC) simulations of this regime we find that the rapid spot-size squeeze event leads to significant consequences. Firstly, a rise in the ponderomotive force drives a sharply rising density perturbation with a corresponding relativistic reduction in plasma frequency, in the increasing intensity. The interplay of these competing effects only affects that part of the laser pulse overlapping with the electron density build-up, in the front region of the bubble. This rapid shift in the group velocity of a part of the laser pulse and the resulting change in its wavelength profile leads to the slicing of the laser longitudinal envelope. This slicing sets the pulse into a state of a strong ‘‘optical shock’’, very similar to states observed in [23]. Secondly, the slicing breaks the oscillatory envelope mode due to the coupling of the transverse dynamics to the longitudinal envelope, not ac-

counted for in our model.

This high-intensity laser pulse slicing effect is a new mechanism driven by the nonlinear envelope oscillations in the strongly mis-matched regime. It is very different from the energy depletion based sharpening of a laser front which is caused by pulse etching [24]. The process of etching is described in the matched regime where whole of the pulse front red-shifts. Slicing on the other hand essentially detaches the head of the pulse from the rest of its body, exciting a strong optical shock.

The effect of a strong optical shock on the acceleration mechanism is shown to be optimal only over a narrow range of densities. At the lower end of this range, the radial squeeze is slow and a weak optical shock is reached close to the laser energy depletion length. At the higher end, the radial squeeze is too short to allow significant interaction between the injected beam and the short-lived peak field. The wavelength of the envelope oscillations is also short, resulting in closely spaced successive laser slicing events. Both these effects inhibit acceleration to the highest energies at higher densities.

In response to the sliced pulse forming a strong optical shock, the bubble elongates resulting in a novel self-injection mechanism and higher peak plasma fields. Beam injected during this elongation experiences the large peak plasma fields and a longer ion cavity.

This work is organized into the following sections. In section II we derive a non-linear envelope equation to show the important laser self-guiding characteristics in the strongly mis-matched regime. In section III a heuristically derived adjusted- a_0 model is used to show that the highest electron energies in the strongly mismatched regime can exceed the predictions of incident a_0 scaling law, in eq.2. In section IV, we use PIC simulations to analyze the evolution of laser-plasma interaction and the physical mechanisms underlying electron acceleration in this regime. Using PIC-based analysis, in IV A we show the excitation of an optical shock and in IV B we present the properties of the accelerated beam in this regime before concluding.

II. NONLINEAR ENVELOPE EQUATION OF LASER IN A BUBBLE-SHAPED PLASMA-WAVE

In this section, we derive a nonlinear envelope equation applicable to the bubble regime to describe the asymmetric oscillations of the laser envelope in the strongly mismatched regime.

An analytical model of the evolution of the laser beam envelope size under laser-excited electron response using individual ray equations of geometric optics in a homogeneous plasma was first modeled in [9]. An envelope equation of the variation of radial envelope size $R_s(z)$ with $z = ct$, was derived in this work (size was defined as the root-mean-square of the radial location of individual rays). It was shown to be of the form of the evolution

equation of a coasting particle beam [12].

This equation which assumes radial symmetry was then simplified using the source dependent expansion with Laguerre-Gaussian eigen-functions, under the assumption, $a_{m=0} \gg a_{m>0}$ (where m is the mode number and represents the order of the Laguerre polynomial and $m = 0$ corresponds to TEM₀₀-mode). The equation thus obtained was then further simplified to determine the self-focusing critical power for TEM₀₀-mode under the asymptotic approximation of a large value of $R_s(z)/(a_{\text{inc}}R_{\text{inc}})$, where R_{inc} is the incident root-mean-square envelope size and a_{inc} is the peak incident normalized vector potential.

In [10], a quasi-static approximation of a driven wave equation in vector potential was used to show that the critical laser power corresponds to the condition of complete expulsion of all electrons from within the laser volume, referred to as electron cavitation.

In eq.3 which models the self-guiding behavior, vacuum diffraction is balanced by laser driven refractive index profile. It however predicts that the envelope undergoes a catastrophic radial collapse for $P > P_c$ and thus this equation was not useful above the threshold.

$$\begin{aligned} \frac{a_{\text{inc}}R_{\text{inc}}}{R_s(z)} &\rightarrow 0 \\ \frac{d^2R_s(z)}{dz^2} &= \frac{R_{\text{inc}}^2}{a_{\text{inc}}^2Z_R^2} \left[\frac{1}{R_s(z)} \left(\frac{a_{\text{inc}}R_{\text{inc}}}{R_s(z)} \right)^2 \left(1 - \frac{P}{P_c} \right) \right] \end{aligned} \quad (3)$$

The above result was obtained using an insightful effective potential approach that modeled the behavior of the envelope by using a simplifying ‘‘single particle’’ model. The location of the particle is set to R_s and the right-hand-side of the envelope equation eq.3 can be written as a normalized effective potential $V(R_s, P/P_c)$, to model the oscillations of this ‘‘particle’’ as in eq.4 [9][11].

$$\begin{aligned} \frac{d^2R_s(z)}{dz^2} &= -\frac{R_{\text{inc}}^2}{a_{\text{inc}}^2Z_R^2} \left(\frac{\partial V_{\text{eff}}}{\partial R_s} \right) \\ V_{\text{eff}}(R_s, P/P_c) &= \frac{1}{2} \left(\frac{a_{\text{inc}}R_{\text{inc}}}{R_s} \right)^2 \left[1 - \frac{P}{P_c} \right] \end{aligned} \quad (4)$$

A different equation was derived in the opposite asymptotic limit of $P/P_c > 1$ and small value of $R_s(z)/(a_{\text{inc}}R_{\text{inc}})$ of the form in eq.5. In this limit, the laser envelope begins to diffract when the spot-size satisfies the condition that $R_s < a_{\text{inc}}R_{\text{inc}}/(16 P/P_c)^{1/3}$ the rate of change of envelope becomes too high for the relativistic effects to continually focus it down. Under this condition the envelope can either oscillate or diffract away depending upon its initial rate of change. However, the solutions of eq.5 are not accurate in the bubble regime.

$$\begin{aligned} \frac{R_s(z)}{a_{\text{inc}} R_{\text{inc}}} &\rightarrow 0 \\ \frac{d^2 R_s(z)}{dz^2} &= \frac{R_{\text{inc}}^2}{a_{\text{inc}}^2 Z_R^2} \left(\frac{1}{R_s(z)} \left(\frac{a_{\text{inc}} R_{\text{inc}}}{R_s} \right)^2 \dots \right. \\ &\quad \left. \left[1 - 16 \frac{P}{P_c} \left(\frac{R_s}{a_{\text{inc}} R_{\text{inc}}} \right)^3 \right] \right) \end{aligned} \quad (5)$$

We use the effective potential on a particle approach under the assumption that the laser spot-size is equal to the Bubble radius, $R_s \simeq R_B$. PIC simulations validate this assumption nearly over the entire length of the evolution of the laser to within a small factor of the order of unity. The sheath surrounding the bubble cavity is effectively the particle in this nonlinear “single particle” model. In the bubble regime, the condition that $P \gg P_c$ and $a_0 \gg 1$, is generally satisfied and therefore the effective potential is not dominated by the interplay between the relativistic focusing and vacuum diffraction. Taking into consideration the catastrophic collapse predicted for $P > P_c$ in eq.4, we retain these terms only when $P \leq P_c$.

In the nonlinear bubble regime, the effective potential is dictated by interplay between the ponderomotive potential and the ion electrostatic potential. So, for $P \geq P_c$, the effective potential is the sum of the ponderomotive potential of the laser pulse in eq.6,

$$\begin{aligned} \phi_p(P, R_s) &= \Phi_p(P, R_s)/(m_e c^2) \\ &= \gamma_{\perp}(P, R_s) - 1 = \sqrt{1 + a^2(P, R_s)} - 1 \end{aligned} \quad (6)$$

where a is the normalized vector potential and the ion cavity potential in eq.7 on the “particle” representing the electron sheath surrounding the laser pulse,

$$\phi_{\text{cav}}(R_s) = \Phi_{\text{cav}}(R_s)/(m_e c^2) = k_{pe}^2 R_s^2/4 \quad (7)$$

where, $k_{pe} = \omega_{pe} c^{-1}$. This gives us the total effective potential and the corresponding non-linear envelope equation, eq.8 respectively. Here \mathcal{H} is the Heaviside step function.

$$\begin{aligned} V_{\text{eff}} \left(R_s, \frac{P}{P_c} \right) &= \frac{1}{2} \left(\frac{a_{\text{inc}} R_{\text{inc}}}{R_s} \right)^2 \left[1 - \frac{P}{P_c} \right] \mathcal{H}(P_c - P) \dots \\ &\quad + (\phi_p(P, R_s) + \phi_{\text{cav}}(R_s)) \mathcal{H}(P - P_c) \\ &= \frac{1}{2} \left(\frac{a_{\text{inc}} R_{\text{inc}}}{R_s} \right)^2 \left[1 - \frac{P}{P_c} \right] \mathcal{H}(P_c - P) \dots \\ &\quad + \left(\sqrt{1 + a^2(P, R_s)} - 1 + \frac{k_{pe}^2 R_s^2}{4} \right) \mathcal{H}(P - P_c) \\ \frac{d^2 R_s(z)}{dz^2} &= \frac{R_{\text{inc}}^2}{a_{\text{inc}}^2 Z_R^2} \times \dots \\ &\quad \left\{ \frac{1}{R_s} \left(\frac{a_{\text{inc}} R_{\text{inc}}}{R_s} \right)^2 \left[1 - \frac{P}{P_c} \right] \mathcal{H}(P_c - P) + \dots \right. \\ &\quad \left. \frac{1}{2} \left[\frac{a^2(P, R_s)}{\sqrt{1 + a^2(P, R_s)}} \frac{1}{(R_s/4)} - k_{pe}^2 R_s \right] \mathcal{H}(P - P_c) \right\} \end{aligned} \quad (8)$$

We note that we have assumed that the radial mode of the laser spot over its evolution remains TEM₀₀ and thus,

$$\begin{aligned} a^2(r, z) &= \frac{a_{\text{inc}}^2 R_{\text{inc}}^2}{R_s^2(z)} e^{-2r^2/R_s(z)^2} \\ \frac{\partial a^2(r, z)}{\partial r} \Big|_{r=R_s} &= \frac{a_{\text{inc}}^2 R_{\text{inc}}^2}{R_s(z)^2} \frac{\partial}{\partial r} e^{-2r^2/R_s^2(z)} = \frac{-4r}{R_s^2} a^2(r, z) \Big|_{r=R_s} \\ \frac{\partial a^2(r, z)}{\partial r} \Big|_{r=R_s} &= -\frac{1}{R_s/4} a^2(r = R_s, z) \end{aligned} \quad (9)$$

From eq.8, the matched spot-size, R_{inc}^m can be inferred to be a critical point. It is the critical incident spot-size where the ponderomotive force pushing the envelope out equals to the electrostatic ionic potential pulling it in and is found to be the same as the matched plasma-wave bubble radius matching condition in eq.1 (under the approximation, $a(r = R_s) \simeq a_{\text{inc}}$ and $\sqrt{1 + a_{\text{inc}}^2} \simeq a_{\text{inc}}$).

$$R_{\text{inc}}^m = w_0 \simeq W_0 = 2\sqrt{a_{\text{inc}}} k_{pe}^{-1} \equiv R_{\text{bubble}} \quad (10)$$

There is an initial radial “velocity” of the envelope for any value of $R_{\text{inc}} \neq R_{\text{inc}}^m$. For $R_{\text{inc}} > R_{\text{inc}}^m$, the ion electrostatic force is dominant and the envelope develops a negative radial velocity initially. Whereas in the opposite limit, $R_{\text{inc}} < R_{\text{inc}}^m$ the ponderomotive force dominates and the envelope particle gains a positive initial radial velocity. Here we deal mostly with negative initial velocity condition because the focal mode-quality is higher for a larger spot-size from experimental considerations, as discussed above.

We note that the local changes in group velocity and wavelength within the laser envelope due to local electron density variations within the frame of the laser pulse are not accounted for in this model. Similarly the depletion of laser energy is not accounted for. As we will later

show using PIC simulations of the strongly mismatched regime, these effects become quite important to the envelope behavior.

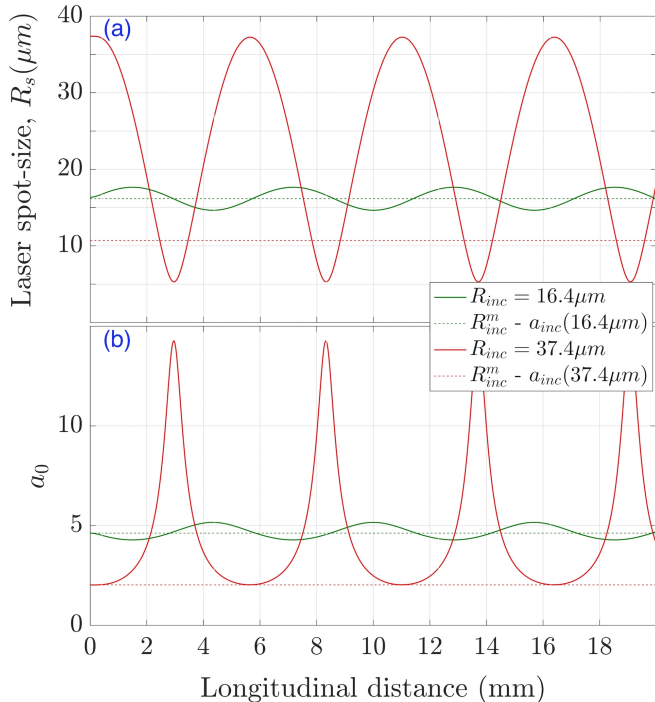


FIG. 1. Solutions of the nonlinear envelope equation, eq.8 showing the effect of the mismatch on laser envelope oscillations by comparing $R_{\text{inc}} = 16.4\mu\text{m}$ and $R_{\text{inc}} = 37.4\mu\text{m}$ at $n_0 = 2 \times 10^{18}\text{cm}^{-3}$. (a) shows the envelope spot-size $R_s(z)$ with longitudinal distance. (b) shows the value of a_0 with longitudinal distance. The dashed horizontal lines show the matched spot-size, R_{inc}^m at the corresponding incident a_{inc} .

Numerical solution of eq.8 are presented in Fig.1 for laser energy of $\mathcal{E}_L = 10J$ and intensity full-width-at-half-of-maximum (FWHM) pulse length $\tau_p = 49\text{fs}$ at electron density $n_0 = 2 \times 10^{18}\text{cm}^{-3}$. The plasma is initialized with a $500\mu\text{m}$ rising plasma density ramp from vacuum to n_0 to model a confined gas source and for consistency with PIC simulations. We compare two different incident spot-sizes, $R_{\text{inc}} = w_0 = 16.4\mu\text{m}$ and $37.4\mu\text{m}$ (with experimentally relevant intensity FWHM spot-sizes of $19.25\mu\text{m}$ and $44\mu\text{m}$ respectively [14][15]) and corresponding $a_0 \sim$ of 4.6 and 2.0 respectively. In Fig.2, the initial focal spot-size is fixed at $R_{\text{inc}} = w_0 = 37.4\mu\text{m}$ and three different densities are compared.

In Fig.1(a) we compare the spot-size evolution for $R_{\text{inc}} = 16.4\mu\text{m}$ (nearly matched for $\mathcal{E}_L = 10J$ and $n_0 = 2 \times 10^{18}\text{cm}^{-3}$, as seen from the matched dashed line) which has a small amplitude sinusoidal evolution and a highly mismatched (by a factor of 4) $R_{\text{inc}} = 37.4\mu\text{m}$. Note that, $R_{\text{inc}} = 37.4\mu\text{m}$ is matched at $n_0 = 1.5 \times 10^{17}\text{cm}^{-3}$. It is evident that with a high degree of mismatch at incidence, the envelope oscillations become asymmetric. It is also seen that in the strongly mismatched regime the a_0 in Fig.1(b) sharply rises to many times its incident

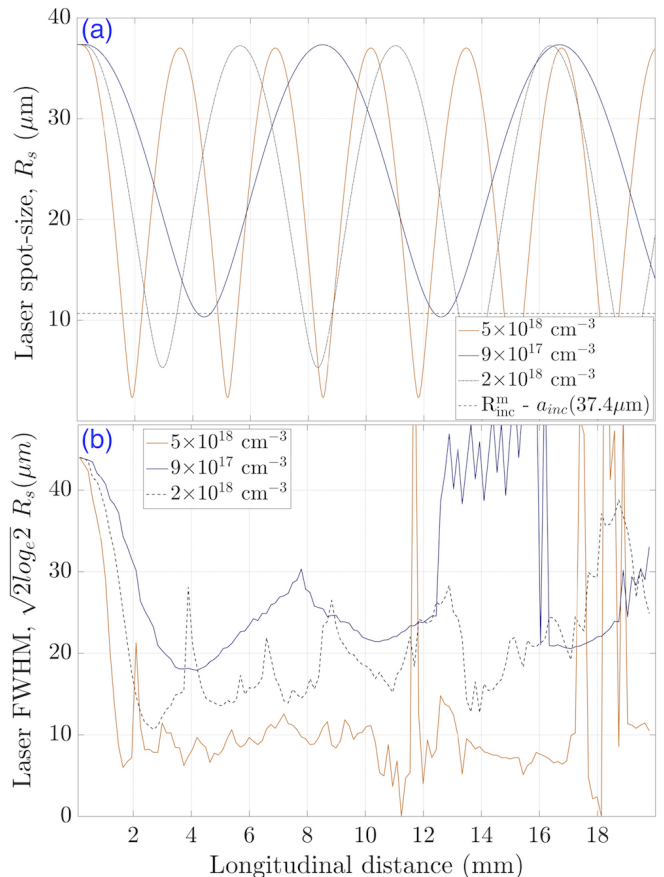


FIG. 2. Solutions of the nonlinear envelope equation, eq.8 for different densities is shown in (a) and compared to the envelope evolution from PIC simulations (described in section IV) in (b). This shows the effect of the variation of the degree of mismatch by varying the plasma density while keeping $R_{\text{inc}} = 37.4\mu\text{m}$ and the other laser parameters the same.

value during the asymmetric radial squeeze phase. This is a critical result, as it implies rapid variation in the laser-driven plasma wave properties.

From the plasma density variation in Fig.2(a), it is seen that at a fixed incident spot-size, the oscillation wavelength and the minima of the spot-size in the squeeze phase of the oscillation becomes smaller at higher densities (higher degree of mismatch), while the asymmetry in the oscillations increases.

This nonlinear envelope equation also gives quantitative comparison to the PIC simulations, as shown in Fig.2(b). The details of PIC simulations are in section IV. From simulations, at $n_0 = 2 \times 10^{18}\text{cm}^{-3}$ for incident spot-size of $w_0 = 37.4\mu\text{m}$, the first radial squeeze minima occurs at around 3mm, as predicted by the numerical solutions of eq.8. The model also correctly predicts the trend of wavelength of spot-size evolution and its minima over a range of densities. However, as it is evident from simulations at the minima of the first radial squeeze, the envelope evolution behavior changes. We would like to note that in PIC simulations each point is 500fs apart

and thus the behavior is not smooth.

Similar asymmetric envelope oscillation behavior has been reported earlier in [25] for sub-critical laser power ($P < P_c$) in a channel-guided mismatched regime, where the incident spot-size is not matched to the matched spot-size for channel-guiding.

It is important to point out that as the radial envelope squeeze phases become shortened and the change in laser envelope radius and a_0 becomes more rapid, in simulations it is important to more carefully resolve the radial dimension. In comparison, the matched-regime simulations place a weaker constraint on the resolution of the radial dimensions. In Fig.1(b) at $n_0 = 2 \times 10^{18} \text{cm}^{-3}$ the value of a_0 varies around its peak over distances which are of the order of $100 - 200 \mu\text{m}$. Similarly, in Fig.2(b), the change in radial size is over a few plasma wavelengths. We thus use fully resolved $2\frac{1}{2}$ D PIC simulations to study this regime instead of transversely under-resolved 3D simulations.

This also opens up the case for a “optical plasma lens”. If the plasma-based focal spot squeezing process is experimentally confirmed to result in a higher focal-spot quality with lesser aberrations compared to vacuum optics, such lens is very attractive. We observe from PIC simulations that the energy loss of the laser over the first squeeze phase is relatively small, allowing the possibility of a mode quality-energy trade-off. This is quite similar but operates based on different physical mechanisms compared to a “beam plasma lens” [26].

III. STRONGLY MISMATCHED REGIME AND THE ADJUSTED- a_0 MODEL

TABLE I. 2 GeV GEMINI laser & e^- beam parameters [14]

$\mathcal{E}_L, \text{FWHM}-\tau_p$	$\simeq 10 \text{ J}, 49 \text{ fs}$
P_L	$\simeq 200 \text{ TW}$
W_{0-y} (y-axis)	$37.4 \mu\text{m}$
W_{0-z} (z-axis)	$44.2 \mu\text{m}$
incident a_0 (a_{inc})	$\simeq 1.9$
$\Delta\mathcal{E}_{\text{peak}}$	2.2 GeV
n_0 (peak energy)	$2 - 3 \times 10^{18} \text{ cm}^{-3}$
P_c	$18.3 - 12.2 \text{ TW}$

We use experimental GeV-scale acceleration results from Poder et. al. [14] ($\simeq 2\text{GeV}$ beam) and Kneip et. al. [15] ($\simeq 1\text{GeV}$ beam), to further quantify and describe the mismatched regime.

The predicted accelerated beam energies (using eq.2) over a range of densities for laser and plasma parameters of the experiment of Poder et. al. [14] (in Table.I) are shown in Fig.3 (the dark blue line for 10J laser energy delivered on target by the GEMINI laser). The peak energies predicted by eq.2 for the experiments of Poder et.al.

with $n_0 = 1.5 - 3 \times 10^{18} \text{ cm}^{-3}$ are $\leq 1\text{GeV}$, whereas the experiments obtained energy $> 2\text{GeV}$. Thus, there is a striking disagreement between the predictions of the 3D simulation based models of [13] and the experimental observations [14].

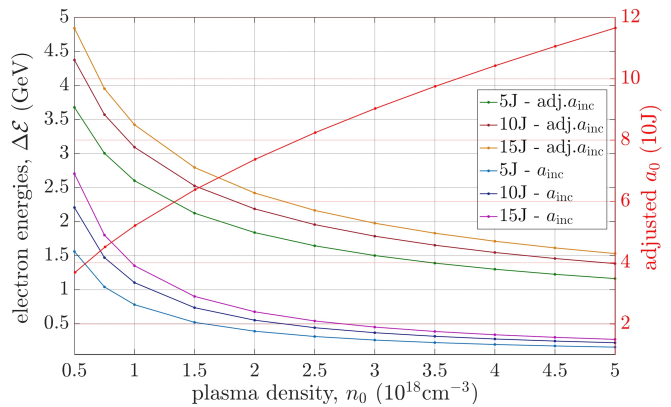


FIG. 3. Comparison of electron beam energies predicted by eq.2 [13] to the energies from the adjusted- a_0 model for laser energies $\mathcal{E}_L=5, 10 \text{ \& } 15 \text{ J}$ (corresponding to parameters in Table.I).

This significant disagreement between the electron energies predicted by eq.2 and the experimentally obtained energies, is because the laser-plasma acceleration process in [14] corresponds to a “strongly mismatched regime”. This is evident from eq.1, the matched w_0 for this interaction at the incident a_0 is $10.3 \mu\text{m}$ and for incident laser energy is $16.4 \mu\text{m}$ at $n_0 = 2 \times 10^{18} \text{ cm}^{-3}$. In contrast, the launched elliptical laser pulse has its smaller waist-size of $37.4 \mu\text{m}$ (a factor of 4 mismatch).

It is important to note that in Poder et. al. [14], the matched spot-size is $16.4 \mu\text{m}$ for a fixed laser energy. However, in the experiments at this matched spot-size the an energy spectral peak is around 800MeV , which is evidenced in [15].

We introduce an “adjusted- a_0 model” which accounts for the mis-match in comparison to the matched-regime energy gain in eq.2 and provides a good agreement with experimental observations. This model assumes that the entire laser pulse energy launched at the entrance of the plasma is coupled into the plasma and is then squeezed down to the matched spot-size corresponding to the launched a_0 . This will therefore increase the a_0 by the factor $w_0(\text{launched})/w_0(\text{matched})$ upon the culmination of the squeezing process for a radially symmetric focal spot. Using these heuristic arguments, energy gain in the *adjusted- a_0 model* is written as in eq.11. F is the optical F-number of the focal spot, $F = \frac{\pi w_0}{2\lambda_0}$. It is related to the F-number of the focusing optics ($F = f/D$, f being the focal length and D being the aperture of the lens).

$$\begin{aligned}
\Delta\mathcal{E}_{\text{adj.}}[m_e c^2] &= \frac{2\pi}{3} \sqrt{a_{0-\text{inc}}} \left(\frac{w_{0-\text{inc}}}{\lambda_0} \right) \sqrt{\frac{n_c}{n_0}} \\
&\simeq 2.5 \sqrt{a_{0-\text{inc}}} \sqrt{\frac{n_c}{n_0}} \text{ F} \\
\text{circ. : } a_0(\text{adj.}) &= a_{0-\text{inc}} \left(\frac{w_{0-\text{inc}}}{w_{0-m}} \right) \\
\text{ellip. : } a_0(\text{adj.}) &= a_{0-\text{inc}} \sqrt{\frac{w_{01-\text{inc}} w_{02-\text{inc}}}{w_{0-m}^2}}
\end{aligned} \tag{11}$$

The adjusted- a_0 model in eq.11 is used to calculate the expected electron energies for parameters of the experiments in [14] (in Table.I) and as seen in eq.12, a good agreement with experimental electron energies is obtained.

$$\begin{aligned}
W_0 &= 37.4\mu\text{m at } 2 \times 10^{18} \text{ cm}^{-3}, \mathcal{E}_L = 10\text{J}, a_0 \simeq 1.9 \\
\Delta\mathcal{E} \text{ (from eq.2)} &: < 1 \text{ GeV} \\
\text{peak expt. } \Delta\mathcal{E} &: 2.2 \text{ GeV} \\
\Delta\mathcal{E} [a_0(\text{adj}) = 7.4] &: 2.2 \text{ GeV}
\end{aligned} \tag{12}$$

For the laser parameters in Table.I, the value of average accelerating plasma field from [13] is $\langle E_{\text{acc}} \rangle(a_0 = 1.9) = 0.5\sqrt{a_0} m_e c \omega_{pe} e^{-1} = 93.7 \text{ GVm}^{-1}$ but with the adjusted- a_0 model it is $\langle E_{\text{acc}} \rangle(a_0[\text{adj.}] = 7.4) = 185 \text{ GVm}^{-1}$. Note that, at $2 \times 10^{18} \text{ cm}^{-3}$, the wave-breaking field is $m_e c \omega_{pe} e^{-1} \equiv E_{\text{wb}} = 136 \text{ GVm}^{-1}$. The adjusted- a_0 model predicts quite correctly even in this case, because in the concerned experiments the peak beam energy of 2.2 GeV is gained over 13mm (not accounting for the injection point). This gives us an average acceleration gradient of $\simeq 170 \text{ GVm}^{-1}$. We find that the peak plasma fields in this regime are of the order of $a_0(\text{adj.}) \times m_e c \omega_{pe} e^{-1} = 1006 \text{ GVm}^{-1}$. Peak fields of around 800 GVm^{-1} are observed in simulations (see Fig.4(b)) where the data is analyzed only every 250 fs.

Not surprisingly, an agreement with the energy-gain predictions of the adjusted- a_0 model is also obtained for experiments reported in Kneip et. al. [15] (see eq.13). At $5.5 \times 10^{18} \text{ cm}^{-3}$ with $a_0 = 3.9$, the matched w_0 is $8.95\mu\text{m}$ whereas the launched $w_0 = 19\mu\text{m}$. The energy expected from the matched regime formula in eq.2 is 510 MeV. The adjusted a_0 -model predicts a beam energy of 957 MeV with $a_0(\text{adj.}) = 8.3$, whereas experimentally a spectral peak was observed at $\simeq 800 \text{ MeV}$.

$$\begin{aligned}
W_0 &= 19.25\mu\text{m at } 5.5 \times 10^{18} \text{ cm}^{-3}, \mathcal{E}_L = 10\text{J}, a_0 = 3.9 \\
\Delta\mathcal{E} \text{ (from eq.2)} &: < 510 \text{ MeV} \\
\text{peak expt. } \Delta\mathcal{E} &: 800 \text{ MeV} \\
\Delta\mathcal{E} [a_0(\text{adj}) = 8.3] &: 957 \text{ MeV}
\end{aligned} \tag{13}$$

In the following sections using PIC simulations it is shown that the heuristic arguments that lead to this good

agreement has its basis in the laser envelope evolution in this regime. The laser energy within the incident spot squeezing down to the matched spot-size and the laser waist subsequently remaining close to the matched spot-size, is shown below to be applicable over a wide range of densities.

But, the not all the processes playing a role in electron acceleration to high energies are not fully incorporated within the adjusted- a_0 model. This reflects in the fact that there are still a few important observations that go against generalizing the arguments used in developing the model:

- (i) Why does this energy scaling only work optimally over densities in the range $n_0 = 1.5 - 3 \times 10^{18} \text{ cm}^{-3}$ for the experiments reported in Poder et.al. [14] ?
- (ii) Why is there a similar optimal density in the range $n_0 = 5 - 7 \times 10^{18} \text{ cm}^{-3}$ for the results reported in Kneip et.al. [15] ?

Is it a result of the squeezing process only working effectively over certain densities or is it some other mechanism that occurs optimally over a certain density range.

It is clear from the above contradictions that the *adjusted- a_0 model* cannot be applied over a broad range of densities. From PIC simulations we investigate the reasons behind this and understand that the envelope squeezing effect occurs for a broad range of densities in comparison to the densities over which the experiments produce peak electron energies. Therefore, there must be another reason for the *adjusted- a_0 model* working only over a small range of densities.

The reasons behind these contradictions are modeled and explained using PIC simulations, discussed in the next section.

IV. PIC SIMULATIONS BASED ANALYSIS OF THE STRONGLY MISMATCHED REGIME

In this section we present results from $2\frac{1}{2}$ D PIC simulations carried out using the EPOCH code [27]. An analysis of the simulations sheds light on the physical processes underlying the acceleration mechanism in the strongly mismatched regime and reveals the complex laser-plasma interaction dynamics accelerating electrons to multi-GeV energies.

A moving simulation box which tracks the laser pulse at its unperturbed plasma group velocity, is used. Laser parameters are in Table I with vacuum- a_0 in simulations being boosted by a factor of 2 to account for the squeeze-phase peak plasma- a_0 expected from the non-linear envelope equation. A cartesian grid is used with 25 cells per laser wavelength (λ_0) in the longitudinal direction and 15 cells per laser wavelength in the transverse. The simulations are initialized with 4 particles per cell. Absorbing boundary conditions are used for both the fields and particles. The laser pulse is incident from the left boundary (using a laser boundary condition) and propagates in $50\mu\text{m}$ of free-space before focussing onto the ho-

mogeneous plasma at the smaller focal spot-size (of the elliptical f/40 focal spot) before the box starts moving. The plasma density has a $500\mu\text{m}$ linear gradient before the homogeneous plasma, to mimic the measured gas-cell electron density profile.

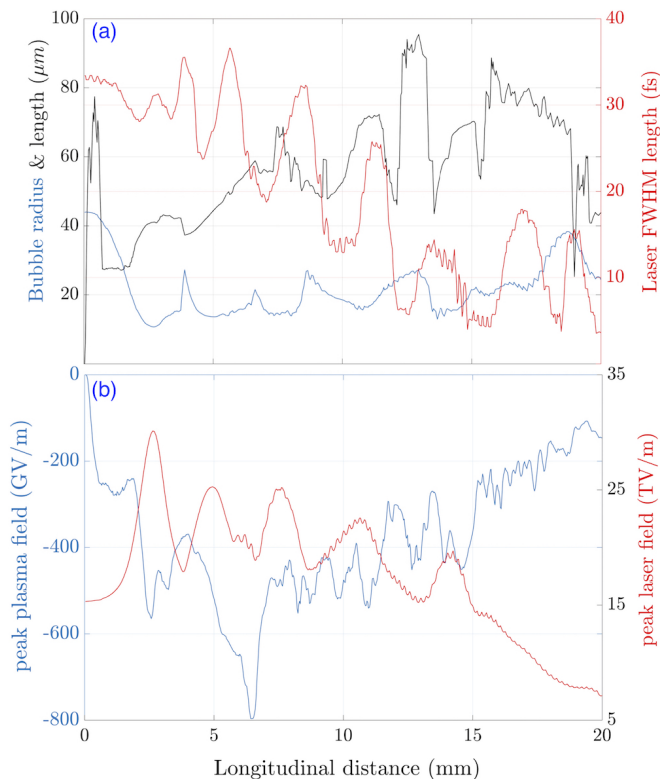


FIG. 4. Results from 2D PIC simulations at $n_0 = 2 \times 10^{18}\text{cm}^{-3}$ showing (a) the evolution of the bubble radial (blue) and length (black) with the laser pulse length from E-field (red) (b) evolution of peak laser field (red) and plasma longitudinal field (blue) with propagation distance using parameters in table I.

We first analyze the evolution of the aggregated laser energy in the simulation box at different densities. The well known laser energy depletion scaling with faster depletion at higher densities is observed. However, the laser energy evolution does not exhibit any correlation with the electron beam energy or possess any specific signature of the underlying laser-plasma interaction process in the mismatched regime. Interestingly, the energy loss over the first “squeeze”-phase is relatively small, allowing this regime to be useful as an efficient *optical plasma lens* and the *adjusted- a_0* model to be valid.

An analysis of the evolution of the laser-plasma dimensions and fields as shown in Fig.4 is much more instructive. Fig.4(a) shows the evolution of dimensions and Fig.4(b) the evolution of fields for $n_0 = 2 \times 10^{18}\text{cm}^{-3}$. There are several interesting laser-plasma effects that can be inferred by studying these evolutions.

These are enumerated below.

- (i) The laser pulse intensity-FWHM waist size (in blue in 4(a)) launched at $44\mu\text{m}$ is squeezed down to a

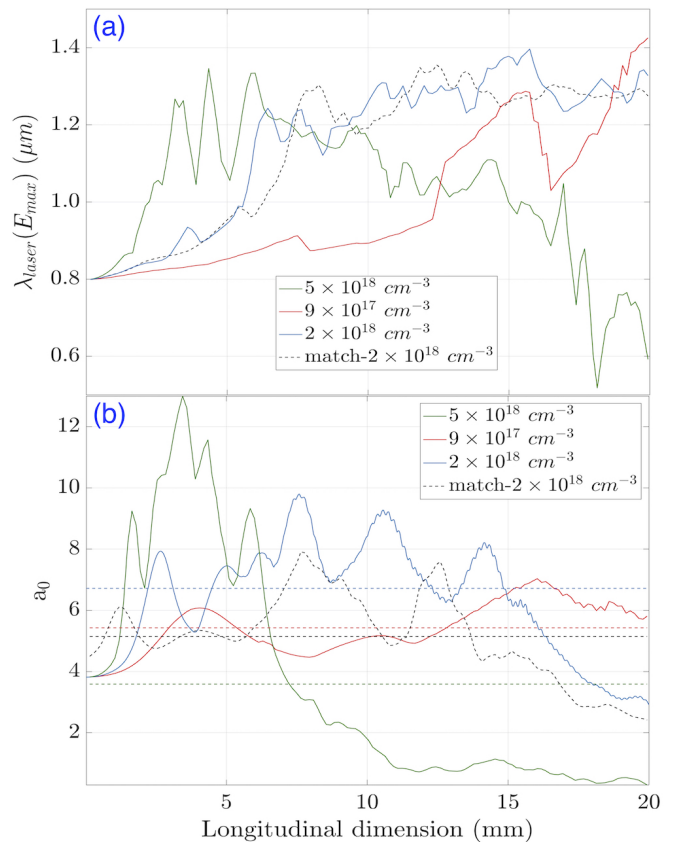


FIG. 5. Results from 2D PIC simulations comparing different densities to show (a) the evolution of laser wavelength at the location of the peak laser field amplitude obtained by averaging the Wigner-ville transform and (b) the evolution of peak laser normalized vector potential obtained using $a_0 \propto \sqrt{I\lambda^2}$.

minimum spot-size of $\simeq 10\mu\text{m}$ in 10 ps ($\simeq 3\text{mm}$). This process of the squeezing down of the initial focal spot to nearly the incident-intensity matched spot-size occurs over a wide range of densities.

- (ii) The laser pulse *radial envelope* oscillates due to the strong initial mismatch. However, the spot-size remains close to the matched spot-size corresponding to the squeezing down of the laser energy to around $15\mu\text{m}$. The maximum radial excursions are less than half the launched spot-size. More importantly these are all precursors to the triggering of a state of “strong optical shock”, which inhibits free radial expansion predicted by the nonlinear envelope equation, eq.8. This radial confinement explains the agreement of the experiments in the strongly mismatched regime to the adjusted- a_0 model, which is based upon the laser energy squeezing to the matched spot-size.
- (iii) The laser pulse longitudinal or temporal envelope undergoes events of “catastrophic collapses”. This is inferred by observing the intensity-FWHM time duration of the laser pulse (in red) over time. There are about 4 such events in 4(a) starting around

4.2mm, 6.3mm, 8.7mm and 12mm. A rapid collapse of the laser time-FWHM indicates the triggering of a strong “optical shock” due to slicing of the laser leading to a sharp laser-front edge.

- (iv) The effect of this laser slicing is observed in a corresponding rapid increase in the bubble length. The length of the bubble is initially equal to its radius. But, as the laser radial envelope squeezes the bubble length suddenly increases while its radius remains nearly constant, as seen by comparing the blue and the black curve (in 4(a)). This is due to the optical shock driving a rapidly elongating bubble.
- (v) The triggering of *optical shock* formation and the excitation of an *elongating bubble* corresponds directly to the injection of electrons in the back of the *elongating* bubble.

The laser-plasma interactions effects driving the acceleration are also evident by observing the evolution of the laser and plasma fields in Fig.4(b). It is observed that the peak plasma field occurs when the laser pulse temporal intensity-FWHM starts undergoing a sudden collapse. The triggering of a strong optical shock drives an elongating bubble with peak plasma field of $\simeq -800$ GV/m at around 6.3mm. The highest energy bunches are injected around this time when the bubble is rapidly elongating in response to the increasing longitudinal ponderomotive force due to the excitation of an optical shock.

$$\mathcal{E}_{quiv}^e(x, r) \propto I(x, r)\lambda_0^2(x, r)$$

$$\text{Spherical bubble : } \nabla_{\parallel} \mathcal{E}_{quiv}^e(x, r) \simeq \nabla_r \mathcal{E}_{quiv}^e(x, r) \quad (14)$$

$$\text{Elongated bubble : } \nabla_{\parallel} \mathcal{E}_{quiv}^e(x, r) \gg \nabla_r \mathcal{E}_{quiv}^e(x, r)$$

This is a novel injection mechanism due to the imbalance between the longitudinal and radial ponderomotive force, a condition represented in eq.14, where $\mathcal{E}_{quiv}^e(x, r)$ is the energy of quiver motion in the laser field. The ponderomotively driven electrons have different longitudinal and radial oscillation periods. The injection occurs due to the lower radial momentum of the electrons pushed by the sliced part of the pulse ahead of the shock, in particular, making them return to the bubble axis much ahead of the electrons driven by the optical shock and experiencing the shock-driven bubble fields.

At 6.3mm (around 24ps) as seen in Fig.4(b) and Fig.6, the optical shock is excited near the peak laser field and the laser energy is still high enough to cause the strongest dis-balance between the radial and longitudinal forces of the laser (see the Supplementary material for the ponderomotive force evolution figure) during its evolution.

A clear insight is also developed into the reasons behind the mismatched regime peaking at an optimal density for delivering the highest energy gain, by referring to Fig.5. In Fig.5(a), the laser wavelength at the maximum laser field is shown for different densities with the optimum being at $n_0 = 2 \times 10^{18} \text{cm}^{-3}$. It is observed that at the lower end of the optimum density range

($n_0 = 9 \times 10^{17} \text{cm}^{-3}$, in red) the wavelength change is slow and a jump in wavelength corresponding to a shock occurs only around 12.5mm, where the laser has depleted significantly. On the other hand, at the higher end of the optimum density range ($n_0 = 5 \times 10^{18} \text{cm}^{-3}$, in green), the triggering of shock occurs multiple times depleting the laser pulse rapidly.

This is further demonstrated by the evolution of peak- a_0 in Fig.5(b) for different densities. At the lower density end of optimum, the value of a_0 increases too slowly and for $n_0 = 9 \times 10^{17} \text{cm}^{-3}$ its average value over 20mm is $\langle a_0 \rangle = 5.4$. At the higher density end of optimum, the value of a_0 increases too rapidly initially and falls to well-below its initial value before 10mm, with the average over 20mm being $\langle a_0 \rangle = 3.6$. For the optimum density at $n_0 = 2 \times 10^{18} \text{cm}^{-3}$ the average value of $\langle a_0 \rangle = 6.7$, which is quite comparable to the value arrived at in the adjusted- a_0 model of 7.4.

In the matched regime which is simulated here with $a_0 \sim 5$ and $w_0 = 16.4 \mu\text{m}$ (the matched parameters used in the nonlinear envelope equation, eq.8 showing minimum envelope oscillations) the rate of wavelength change is much slower than in the mismatched regime. The average value of a_0 in the matched regime over 20mm is much lower in the matched regime at $\langle a_0 \rangle = 5.1$ compared to the optimum for the mismatched regime at $\langle a_0 \rangle = 6.7$.

Here the wavelength is calculated by performing the Wigner-Ville transform of the laser-field on-axis line-out and averaging the resulting wavelength distribution function at each of the longitudinal location. The value of normalized vector potential a is calculated at each location by using its dependence on $I\langle\lambda\rangle^2$ and the peak value is used as a_0 .

A. Strong optical-shock excitation by slicing of the laser longitudinal envelope

We analyze the *triggering* of an optical shock excitation by the evolving dynamics of the laser envelope in the strongly mismatched regime. In this regime, due to the oscillations of the laser radial envelope each of the asymmetric envelope-squeeze event driving the laser radial envelope towards the matched spot-size causes a large surge in the laser electric field. We show that each of the surge in the laser electric fields triggers an *optical shock excitation* event.

$$\beta_g = \beta_{\phi-las}^{-1} \simeq \beta_{g0} \left[1 + \frac{1}{2\gamma_{g0}^2 \beta_{g0}^2} \left(\langle a_{\perp} \rangle^2 - \frac{\delta n}{n_0} \right) \right]$$

$$\beta_{g0} = \sqrt{1 - \frac{\omega_{pe}^2}{\omega_0^2}}, \gamma_{g0} = \frac{\omega_0}{\omega_{pe}} \quad (15)$$

The third-order perturbative expansion based relation for the laser pulse group velocity [28] in a quasi-static plasma wake with local parameters of plasma

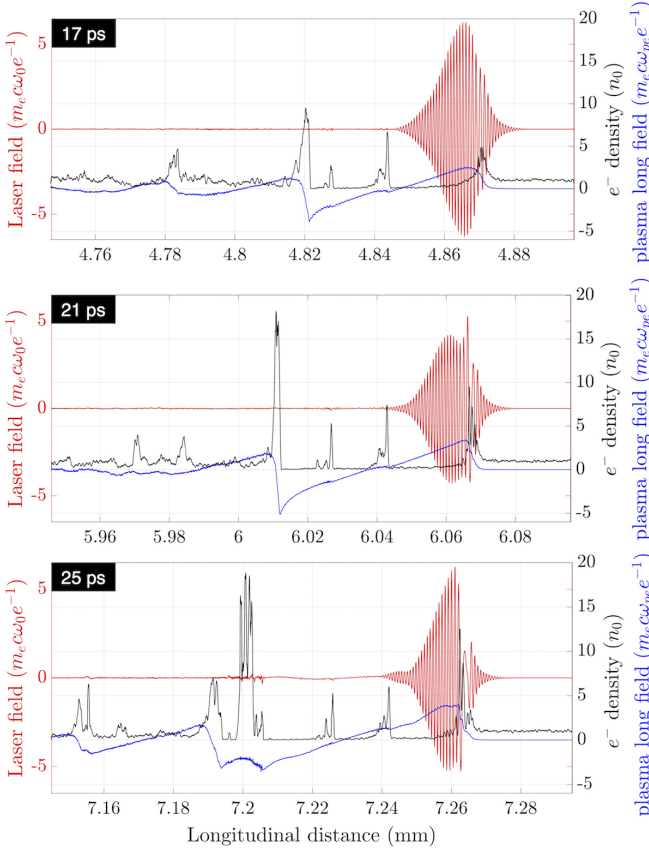


FIG. 6. On-axis line-out from 2D PIC simulations for $n_0 = 2 \times 10^{18} \text{cm}^{-3}$ showing the formation of the optical shock in the strongly mismatched regime. The red curve is the on-axis laser transverse electric field. The plasma longitudinal field (blue curve) can be used to infer the bubble length, which is seen undergoing an increase. The on-axis electron density is in black.

$(\delta n(\xi, r)/n_0)$ and laser $(a(\xi, r))$ dictating the local group velocity as in eq.15 ($\xi = c\beta_{g0}t - z$, is a co-moving coordinate to the propagating laser). This equation is used to treat spatially-localized laser-plasma interaction at each instant of the simulation, because it handles group velocity $\beta_g(\xi, r)$ at each point in space in the co-moving coordinate.

This relation in eq.15 can also be used to estimate a *locally zero group velocity* condition shown in eq.16.

$$\beta_g(\xi, r) = 0$$

$$\frac{1}{2} \left(\frac{\delta n}{n_0} - \langle a_{\perp} \rangle^2 \right) \simeq \frac{n_c}{n_0} \quad (16)$$

Though the local envelope velocity being zero is a mathematical construct, essentially because in this work the typical initial plasma density is around $n_c/n_0 \simeq 30$, it does demonstrate that the group velocity of a pulse in different parts of the wake can be significantly different. It is quite evident that if $\delta n(\xi, r) \rightarrow n_c$ when $\langle a_{\perp}(\xi, r) \rangle^2 \rightarrow 0$, then the local group velocity, $\beta_g(\xi, r) \rightarrow 0$. This implies

that a part of the envelope can be slowed down much more in comparison to the rest of the pulse and thus a part of the envelope can be lost leading to “slicing of the laser” into two distinct pulses under the conditions above. It should also be noted that the $\beta_g(\xi, r) \rightarrow 0$ implies $\beta_{\phi-las}(\xi, r) \rightarrow \infty$ which means $\lambda_{las}(\xi, r) \rightarrow \infty$. So, increasing wavelength in a local region implies a local reduction in the group velocity.

The time evolution of the on-axis laser field from PIC simulations is shown for one such event in Fig.6 which corresponds to the triggering of an optical shock at 21ps and its formation based on the completion of slicing at 25ps. The corresponding rapid increase in the laser wavelength for $n_0 = 2 \times 10^{18} \text{cm}^{-3}$ is also observed in the average wavelength plotted in the Fig.5(a), where around 21ps the laser wavelength has rapidly jumped to $1.2 \mu\text{m}$, from the initially launched value of $0.8 \mu\text{m}$.

The laser-plasma dynamics leading to “laser slicing” is better understood by simultaneously observing and comparing the radial intensity-FWHM in Fig.4(a), the laser field in Fig.4(b), and the laser wavelength in Fig.5(a), while observing the on-axis laser-plasma dynamics in Fig.6.

Now we concentrate on the laser-plasma interaction dynamics in the front of the bubble in Fig.6. It can be seen that at 17ps the wavelength in the front of the wake, a region where there is $\max-\delta n/n_0$ (where the longitudinal ponderomotive force is the highest), begins to lengthen. This time also corresponds to a rapid surge in the laser electric field and thus the ponderomotive force is rapidly increasing. This also leads to an increase in the $\max-\delta n/n_0$ at the laser head. At 21ps, in the region of $\max-\delta n/n_0$ the wavelength has significantly stretched. This corresponds to a rapid reduction in the local group velocity. At 25ps, we observe that the laser envelope is broken into two distinct regions separated by a long wavelength, low group velocity cycle. These laser cycles of long-wavelength low group-velocity lead to the head of the laser pulse detaching from it and triggering the laser into an optical shock state. The duration of the triggered *slicing* of a laser is also the time where the laser longitudinal ponderomotive force becomes largely imbalanced with the radial ponderomotive force.

The large imbalance between the longitudinal and the radial ponderomotive force is seen to have a direct effect on the length and the radial envelope of the laser. The bubble length is seen to grow much more than the bubble radius. The large longitudinal ponderomotive force leading to an elongated bubble has a direct effect on the peak longitudinal plasma field which grows to around -800GV/m at 25ps, as seen in Fig.4(b).

The bubble elongation following an optical shock excitation is the main reason for the self-injection of large charge close to the bubble axis, in the strongly mismatched regime. Because the injection of charge occurs when the laser is in the state of an optical shock, the injected charge experiences the peak plasma field and accelerates to peak energies in about a centimeter. The

elongated bubble also has a longer de-phasing length, thus allowing for slower de-phasing, while it lasts in the elongated state.

B. Beam properties driven by strong optical-shock based self-injection

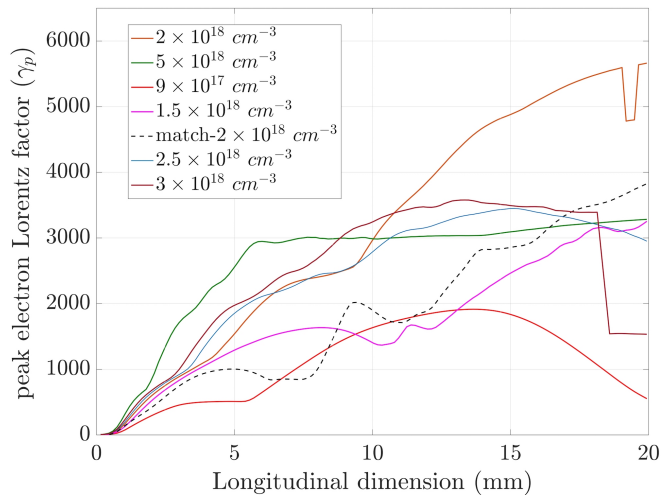


FIG. 7. Evolution of the peak Lorentz factor (γ_p) of electrons which corresponds to the energy gain, $\Delta\mathcal{E}$ compared for various densities and to the matched regime, from 2D PIC simulations of the strongly mismatched regime with laser energy $\mathcal{E}_L = 10\text{J}$.

We present the properties of the accelerated electrons that are injected by the novel strong “optical-shock” driven “elongating bubble” with the GEMINI f/40 parameter set. Due to multiple injection events in the *strongly mismatched regime* the particle stream can only be loosely-termed as a beam. There is a strong dependence of plasma-wave phase velocity and plasma-wave dimensions on the instantaneous laser field amplitude which in turn depends upon the non-linear response of the plasma electrons being driven by the laser. In the strongly mismatched regime we see that the laser and the bubble properties critically depend upon the plasma density and the degree of mismatch due to the reasons elaborated above and thus beam properties reflect this.

In Fig.7, the longitudinal evolution of a property applicable in the realm of laser acceleration is plotted. It is the peak Lorentz factor of the accelerated electrons or indirectly the kinetic energy of the most energetic electrons. It is observed that the peak Lorentz factor clearly has two distinct phases which are represented in the two *different slopes* of the parabolic evolution of peak Lorentz factor with the longitudinal dimension. The parabolic shape is the characteristic of the integration over a linearly decreasing accelerating electric field as the beam gains energy over the back half of the bubble ($\partial\gamma_p/\partial\xi \propto e \times E_{\parallel}^0(1 - \xi/R_B(\xi, t))$, where E_{\parallel}^0 is the

peak field in the back of bubble).

The first energy-gain slope is observed until around 25ps, until the first set of injected particles over-run the accelerating phase of the wake due to bubble expansion and thus stop gaining energy. The second slope is observed after 25ps (after optical shock driven injection event around 24ps) where the peak Lorentz factor rises to $\gamma_p > 3000$ for $n_0 = 1.5 - 3.0 \times 10^{18}\text{cm}^{-3}$ and $\gamma_p > 4000$ for $n_0 \simeq 2 \times 10^{18}\text{cm}^{-3}$. The second energy gain slope is much higher or steeper due to the larger peak plasma fields excited by the strong optical-shock. In the matched regime (shown with a black dotted line), the maximum energy gain is limited to less than 2GeV.

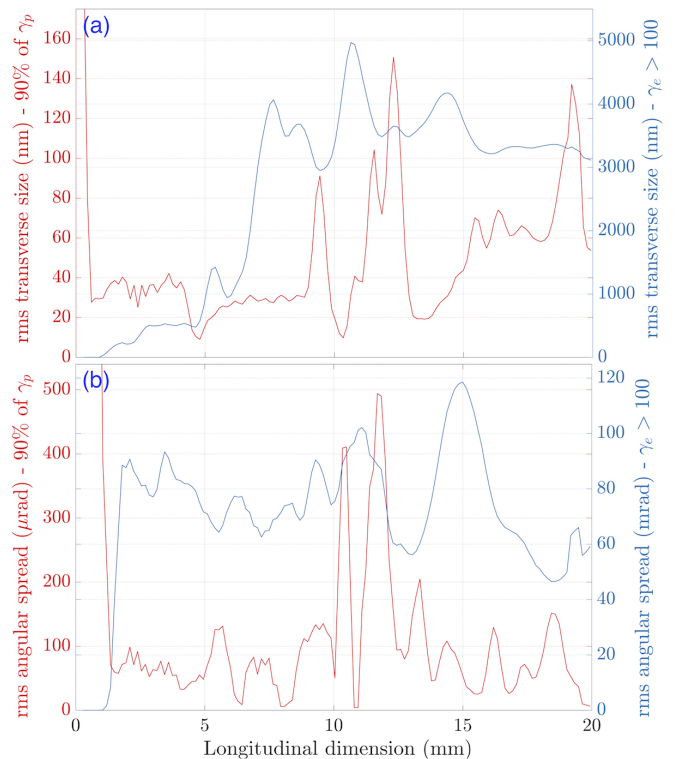


FIG. 8. Beam root-mean-square (rms) transverse-size (in a) and angular-size (in b) evolution with laser propagation distance at $n_0 = 2 \times 10^{18}\text{cm}^{-3}$ from 2D PIC simulations.

In Fig.8(a), the root-mean-square (rms) beam transverse size and Fig.8(b), the root-mean square beam angle are presented corresponding to optimum energy gain case for $n_0 = 2 \times 10^{18}\text{cm}^{-3}$. There are two different metrics which are plotted for both these parameters. These two metrics are necessary because the accelerated electrons are spread over a large volume of the full 6D phase-space it is hard to properly define σ_r and σ_{θ} for laser accelerated electrons. This is unlike the beams from conventional RF cavity based accelerators with a low-energy spread. The first metric we have adopted takes into account all the particle with $\gamma > 100$ and second metric only looks at all the particles with $\gamma > 0.9 \times \gamma_p$. So, the second metric is tuned towards understanding the properties of the highest energy particles.

The rms-size in the y-direction for the component of the beam with the highest energy particles (within 90% of γ_p , where γ_p evolves as shown in Fig.7) is around an average of 50 nm, through most of the evolution. However around the exit the beam transverse size is closer to 100nm for the multi-GeV beam ($\gamma_p \simeq 5500$ for $n_0 = 2 \times 10^{18} \text{cm}^{-3}$ at an interaction length of 20mm). The rms-size in the y-direction for all the particles with $\gamma > 100$ is on average around $3.5 \mu\text{m}$.

The rms-angle (using $\sqrt{\langle p_y^2 \rangle / \langle p_x^2 \rangle} \equiv \sqrt{\langle p_{\perp}^2 \rangle / \langle p_{\parallel}^2 \rangle}$) for the component of the beam with the highest energy particles is around $100 \mu\text{rad}$. Whereas the rms-angle for the particles with $\gamma > 100$ is on average around 80 mrad .

The effective geometrical emittance for the high-energy component of the beam is $\varepsilon_p = \text{rms-}y_p \times \text{rms-}\theta_p \simeq 10^{-5} \text{ mm-mrad}$. The corresponding normalized emittance $\varepsilon_{p-n} = \gamma_p \times \varepsilon_p = 0.04 \text{ mm-mrad}$. The observation of distinct properties of the particles at the peak energy in comparison to all particle above 50 MeV points towards the *adiabatic damping* effect of the geometrical emittance of particles as they undergo acceleration in the plasma. It is also interesting to note the conservation of the emittance of the highest energy particles of the beam, which can be qualitatively seen by the anti-correlation between the rms- y_p and rms- θ_p in Fig.8(a) and (b). Thus, the multi-GeV component of the laser-plasma accelerated beam in the strongly mismatched behaves like a high-quality conventional particle beam.

V. CONCLUSION

We have presented the first detailed theoretical and computational analysis of a strongly mis-matched self-guiding regime of laser-plasma electron acceleration. The underlying physical mechanisms of beam injection and acceleration in this regime are shown to be sig-

nificantly different from the widely accepted matched regime model. The effectiveness of the mis-matched regime is widely evidenced by important experimental results including recent ones on multi-GeV acceleration, for acceleration to higher energies. It has been shown using a nonlinear envelope equation that the envelope oscillations exhibit an asymmetric behavior with shorter squeeze phases and their role in triggering a strong optical-shock excitation has been established. The excitation of a strong optical-shock significantly differentiates the acceleration processes in comparison to the matched regime as it has been shown to results in a rapidly elongating bubble shape. This elongation leads to a unique self-injection method which injects a high-quality trapped beam into the much higher peak accelerating fields and longer accelerating region of the elongated bubble. These results become attractive from a practical perspective as they pave a pathway for scaling to higher electron energies. Thus launching larger focal spot laser pulses in the strongly mismatched self-guiding regime based upon the underlying acceleration mechanisms uncovered here is a novel approach towards high energy beams with large self-injected charge of high quality and higher overall efficiency.

ACKNOWLEDGEMENT

We acknowledge funding from STFC for the support of the John Adams Institute of Accelerator Science by grants ST/J002062/1 and ST/P000835/1. The EPOCH code used in this research was developed under UK Engineering and Physics Sciences Research Council grants EP/G054940/1, EP/G055165/1 and EP/G056803/1. All simulations were carried using the Imperial High Performance Computing systems.

-
- [1] Tajima, T., Dawson, J. M., *Laser Electron Accelerator*, **Phys. Rev. Lett.** **43**, pp.267-270 (1979), doi: 10.1103/PhysRevLett.43.267.
 - [2] Pukhov, A., Meyer-ter-Vehn, J., *Laser wake field acceleration: the highly non-linear broken-wave regime* **J. Appl Phys B** (2002) **74**: 355., doi: 10.1007/s003400200795.
 - [3] Mangles, S. P. D., Murphy, C. D., Najmudin, Z., Thomas, A. G. R., Collier, J. L., Dangor, A. E., Divall, E. J., Foster, P. S., Gallacher, J. G., Hooker, C. J., et. al., *Monoenergetic beams of relativistic electrons from intense laser-plasma interactions*, **Nature** **431**, 535 (2004), doi:10.1038/nature02939.
 - [4] Faure, J., Glinec, Y., Pukhov, A., Kiselev, S., Gordienko, S., Lefebvre, E., Rousseau, J.-P., Burgy, F. and Malka, V., *A laser-plasma accelerator producing monoenergetic electron beams*, **Nature** **431**, 541 (2004), doi:10.1038/nature02963.
 - [5] Pukhov, A., Gordienko, S., *Scalings for ultrarelativistic laser plasmas and quasimonoenergetic electrons*, **Physics of Plasmas** **12**, 043109 (2005), doi: 10.1063/1.1884126.
 - [6] Siegman, A. E., *Defining, measuring, and optimizing laser beam quality*, **Proc. SPIE 1868**, *Laser Resonators and Coherent Optics: Modeling, Technology, and Applications*, **2** (1993), doi 10.1117/12.150601; Siegman, A. E., *How to (Maybe) Measure Laser Beam Quality*, **DPSS (Diode Pumped Solid State) Lasers: Applications and Issues**, *Optical Society of America*, Vol. 17,1998, paper MQ1
 - [7] J-C. Chanteloup, F. Druon, M. Nantel, A. Maksimchuk, G. Mourou, *Single-shot wave-front measurements of high-intensity ultrashort laser pulses with a three-wave interferometer*, **Optics Letters** **23**, iss. 8, pp. 621-623 (1998); Druon, F., Cheriaux, G., Faure, J., Nees, J., Nantel, M., Maksimchuk, A., Mourou, G., Chanteloup, J-C., Vdovin, G., *Wave-front correction of femtosecond terawatt lasers by deformable mirrors*, **Opt. Lett.** **23**, pp.1043-1045 (1998)
 - [8] Max, C. E., Arons, J., Langdon, A. B., *Self-Modulation and Self-Focusing of Electromagnetic Waves in Plasmas*, **Phys. Rev. Lett.** **33**, 209, (1974), doi: 10.1103/PhysRevLett.33.209.
 - [9] Sprangle, P., Cha-Mei Tang ; E. Esarey *Relativistic Self-Focusing of Short-Pulse Radiation Beams in Plasmas*, **IEEE Transactions on Plasma Science**, Vol. 15, Iss. 2, pp.145-153 (1987), doi: 10.1109/TPS.1987.4316677.

- [10] Sun, G. Z., Ott, E., Lee, Y. C., Guzdar, P., *Self-focusing of short intense pulses in plasmas*, *Phys. of Fluids* **30**, 526 (1987), doi: 10.1063/1.866349.
- [11] Hafizi, B., Ting, A., Sprangle, P., Hubbard, R. F., *Relativistic focusing and ponderomotive channeling of intense laser beams*, *Phys. Rev. E* **62**, 4120, (2000), doi:10.1103/PhysRevE.62.4120.
- [12] Kapchinsky, I. M. and Vladimirovsky, V. V., *Limitations of proton beam current in a strong focusing linear accelerator associated with the beam space charge*, *Proc. Int. Conf. on High-Energy Accelerators and Instrumentation*, CERN, Geneva, pp. 274-288, (1959).
- [13] Lu, W., Tzoufras, M., Joshi, C., Tsung, F. S., Mori, W. B., Vieira, J., Fonseca, R. A., Silva, L. O., *Generating multi-GeV electron bunches using single stage laser wakefield acceleration in a 3D nonlinear regime*, *Physical Review Special Topics - Accelerators and Beams* **10**, 061301 (2007), doi:10.1103/PhysRevSTAB.10.061301.
- [14] Poder, K., *Characterisation of self-guided laser wakefield accelerators to multi-GeV energies*, Chapter 7, Ph.D. Thesis, submitted to the Department of Physics, Imperial College London, UK
- [15] Kneip, S., et. al., *Near-GeV Acceleration of Electrons by a Nonlinear Plasma Wave Driven by a Self-Guided Laser Pulse*, *Phys. Rev. Lett.* **103**, 035002 (2009), doi:10.1103/PhysRevLett.103.035002
- [16] Wang, X., Zgadzaj, R., Fazel, N., Li, Z., et. al., *Quasi-monoenergetic laser-plasma acceleration of electrons to 2 GeV*, *Nature Communications* **4**, 1988 (2013)
- [17] Golovin, G., Chen, S., Powers, N., Liu, C., Banerjee, S., et. al. *Tunable monoenergetic electron beams from independently controllable laser-wakefield acceleration and injection*, *Phys. Rev. ST Accel. Beams* **18**, 011301 (2015)
- [18] Kim, H. T., Pathak, V. B., Pae, K. H., Lifschitz, A., et. al., *Stable multi-GeV electron accelerator driven by waveform-controlled PW laser pulses*, *Scientific Reports* **7**, 10203 (2017)
- [19] E. Brunetti, R. P. Shanks, G. G. Manahan, M. R. Islam, B. Ersfeld, et. al., *Low Emittance, High Brilliance Relativistic Electron Beams from a Laser-Plasma Accelerator*, *Phys. Rev. Lett.* **105**, 215007 (2010)
- [20] Beaurepaire, B., Vernier, A., Bocoum, M., Bohle, F., Jullien, A., Rousseau, J-P., Lefrou, T., Douillet, D., Iaquaniello, G., Lopez-Martens, R., Lifschitz, A., Faure, J., *Effect of the Laser Wave Front in a Laser-Plasma Accelerator*, *Phys. Rev. X* **5**, 031012 (2015)
- [21] Jacobi, C. G. J., *Fundamenta Nova Theoriae Functionum Ellipticarum*, Königsberg, Germany: Regiomonti, Sumtibus fratrum Borntraeger, 1829; Chandrasekharan, K., *Elliptic Functions*, Berlin: Springer-Verlag, 1985, ISBN-10: 0387152954
- [22] Korteweg, D. J. and de Vries, G., *On the Change of Form of Long Waves Advancing in a Rectangular Canal, and on a New Type of Long Stationary Waves*, *Philosophical Magazine* **39**, 240, pp.422-443, (1895). doi:10.1080/14786449508620739
- [23] Gaeta, A. L., *Catastrophic Collapse of Ultrashort Pulses*, *Phys. Rev. Lett.* **84**, 3582, (2000), doi:10.1103/PhysRevLett.84.3582
- [24] Decker, C. D., Mori, W. B., Tzeng, K. C., T. Katsouleas, *The evolution of ultra-intense, short-pulse lasers in underdense plasmas*, *Physics of Plasmas* **3**, 2047 (1996)
- [25] Ehrlich, Y., Cohen, C., Zigler, A., Krall, J., Sprangle, P. and Esarey, E., *Guiding of High Intensity Laser Pulses in Straight and Curved Plasma Channel Experiments*, *Phys. Rev. Lett.* **77**, 4186, (1996)
- [26] Chen, P., *Plasma Focusing of High energy beams*, SLAC-PUB-4049, August 1986
- [27] T D Arber, K Bennett, C S Brady, et. al. *Contemporary particle-in-cell approach to laser-plasma modelling*, *Plasma Phys. Control. Fusion* **57**, 113001, (2015)
- [28] Sahai, A. A., *On Certain Non-linear and Relativistic Effects in Plasma-based Particle Acceleration*, Ph.D. dissertation, Duke university, July 2015